

# Establishment of Dynamic Model of axle Box Bearing of high-speed Train under Variable Speed Conditions

Yongqiang Liu (✉ [liyq@stdu.edu.cn](mailto:liyq@stdu.edu.cn))

Shijiazhuang Tiedao University

**Baosen Wang**

Shijiazhuang Tiedao University

**Bin Zhang**

University of South Carolina College of Engineering and Computing

**Shaopu Yang**

Shijiazhuang Tiedao University

---

## Research Article

**Keywords:** Variable speed conditions, High-speed train, Bearing model, Angle iteration, Order ratio spectrum

**Posted Date:** July 7th, 2021

**DOI:** <https://doi.org/10.21203/rs.3.rs-656308/v1>

**License:**  This work is licensed under a Creative Commons Attribution 4.0 International License.

[Read Full License](#)

---

# Establishment of dynamic model of axle box bearing of high-speed train under variable speed conditions

Yongqiang Liu<sup>1,\*</sup>, Baosen Wang<sup>2,3</sup>, Bin Zhang<sup>3</sup>, Shaopu Yang<sup>4</sup>

1. School of Mechanical Engineering, Shijiazhuang Tiedao University, Shijiazhuang, 050043, China.

2. School of Traffic and Transportation, Shijiazhuang Tiedao University, Shijiazhuang, 050043, China.

3. College of engineering and computing, University of South Carolina, Columbia, South Carolina, 29208, America.

4. State Key Laboratory of Mechanical Behavior and System Safety of Traffic Engineering Structures, Shijiazhuang Tiedao University, Shijiazhuang 050043, China.

\*corresponding author: Yongqiang Liu; liuyq@stdu.edu.cn

---

## Abstract

This paper establishes a dynamic model of the bearing rotor system of a high-speed train under variable speed conditions. Different from previous works, the proposed model simplifies the contact stress and considers the compensation balance excitation caused by the rotor mass eccentricity. The angle iteration method is used to solve the challenging problem that the roller space position cannot be determined in bearing rotation. The simulation results show that the model accurately describes the dynamics of bearing under varying speed profiles that contain acceleration, deceleration and speed oscillation stages. The order ratio spectrum of the bearing vibration signal indicates that both single frequency and multiple frequency in simulation results are consistent with that in theoretical results. Experiments of bearing with outer ring fault and inner ring fault under various operating conditions are presented to verify the developed model.

*Keywords:* Variable speed conditions, High-speed train, Bearing model, Angle iteration, Order ratio spectrum

---

## 1. Introduction

2 In recent years, with the rapid development of high-speed railways, the  
3 global high-speed railway mileage and the number of trains increased rapidly,

4 which make safe and reliable operation of train critical to railway safety [1, 2].  
5 As key components of train running systems, bogie axle box bearings have  
6 attracted extensively studies on movement modeling and state monitoring  
7 [3]. To better understand the mechanism of bearing faults and their effects  
8 on movement, dynamic simulation of bearing systems are commonly used.  
9 The bearing model studies the influence of parameters on bearing motion  
10 states by establishing a set of differential equations, which can be solved by  
11 using numerical solution methods.

12 In the early stage of research, relatively simple nonlinear equations were  
13 used to simulate bearing motion, and study the motion law of bearings based  
14 on the exact solutions of these equations. For instance, Chinta [4] used non-  
15 dimensional differential equations to describe the unbalanced response of  
16 rotor bearings, and used Floquet theory to study the stability and bifurcation  
17 behavior of bearing systems. Sinou [5] established a dynamic model of a  
18 flexible rotor-rolling bearing system under unbalanced excitation, used the  
19 harmonic balance method to study the system's nonlinear motion law, and  
20 analyzed the influence of bearing radial clearance and unbalanced mass on  
21 Hertzian contact force between roller and raceway.

22 Since traditional nonlinear equation solving methods can only obtain ap-  
23 proximate solutions of nonlinear system with fewer degree of freedom (DOF),  
24 some more advanced methods were developed for higher DOF bearing sys-  
25 tems. Fukata and Gad et al [6] used a numerical method to solve the dif-  
26 ferential equations of ball bearing motion for the first time, and intuitively  
27 analyzed the motion state of bearings. Tiwari and Gupta et al [7] estab-  
28 lished a nonlinear dynamic model of bearing rotor systems, and analyzed the  
29 influence of radial clearance on the motion stability based on the Floquet  
30 theory. Sawalhi et al [8] built a dynamic model of bearing and gear cou-  
31 pling system, in which a small sprung mass with relatively high damping is  
32 used to represent a typical high frequency. Furthermore, the model is ver-  
33 ified through experiments under different fault conditions [9]. Tsuha et al  
34 [10] developed a rolling bearing model with improved fidelity by introducing  
35 a set of equivalent contact stiffness and damping and using the theory of  
36 elastic fluid lubrication to calculate the contact force. Song [11] put forward  
37 a dynamic model of spindle bearing systems by combining angular contact  
38 bearing and floating bearing. Compared with transitional methods, these  
39 advanced methods consider more factors that affect bearing motion, so the  
40 established bearing motion model is more accurate. At the same time, the  
41 numerical solution method makes the solution of the equation more intuitive

42 and provides great convenience for further nonlinear analysis. However, these  
43 works focus on bearing under constant operating conditions, which cannot  
44 sufficiently describe the dynamics operating conditions.

45 Different from those bearings working in relatively consistent operating  
46 conditions, high-speed train bearings in the running system often work in  
47 high-speed and heavy-duty harsh conditions and are severely affected by  
48 strong noises in the surrounding environment. It is difficult to directly eval-  
49 uate the quality of the bearings and study the bearing motion states. To  
50 address these challenges, the dynamic model simulation methods are desired  
51 for bearings of high-speed trains. The method of dynamic modeling should  
52 consider the influence of various factors on the motion states of bearings,  
53 greatly reducing the research cost, and improving the research efficiency. Cao  
54 et al [12] established a nonlinear dynamic model of the CRH1 EMU (China  
55 Railway High-speed-1, Electric Multiple Units) coupling system, which con-  
56 siders the loose fit between the inner ring and the main shaft of the axle box  
57 bearing of the high-speed train. They also studied and compared the motion  
58 characteristics of the model by using optimized numerical algorithms under  
59 various working conditions. Cao and He et al [13] established a dynamic  
60 model of high-speed rolling bearings by considering actual factors such as  
61 centrifugal expansion and thermal expansion of the inner ring. The model  
62 was then used to predict some system parameters such as contact angle and  
63 bearing stiffness and conduct correlative analysis of bearing damage mech-  
64 anism. Yang et al [14] established a 4 DOF nonlinear dynamic model with  
65 classic fault of high-speed train bearing-rotor systems. The model was ver-  
66 ified by a certain type of high-speed train bearing under outer ring, inner  
67 ring and roller element fault conditions. Liu et al [15] established a 12 DOF  
68 non-linear dynamic model of high-speed train axle box bearings with outer  
69 ring faults, in which the influence of bearing speed and fault size on system  
70 motion was studied from a nonlinear perspective. Wang et al [16] proposed  
71 a novel stochastic vehicle-track coupled model to evaluate the dynamic per-  
72 formance of axle box bearings in a high-speed train with unsteady wind load  
73 and random track irregularities and study the influence of crosswind speed  
74 on dynamic performance of bearings.

75 With these successes in bearing model research, the limitation of existing  
76 works, however, is that failure mechanism and bearing motion are all studied  
77 with static bearing speed. Mishra et al [17] established a bond graph model  
78 of rolling element bearings in special operating conditions, and verified the  
79 effectiveness through experiments [18]. The main function of this model

80 is to generate a series of non-stationary signals for fault diagnosis algorithm  
81 research. However, this model cannot describe the vibration response of each  
82 part of bearing rotor systems. Moreover, these bearing models have a single  
83 structure, which is insufficient to represent the structural characteristics of  
84 tapered roller bearings of high-speed trains. Furthermore, in addition to the  
85 bearing mass eccentricity, the shaft mass eccentricity is also very important  
86 but is always ignored in bearing rotor systems. To address these limitations,  
87 this paper establishes a dynamic model of coupling systems of bearing and  
88 shaft to accurately simulate the dynamics of real axle box bearings of high-  
89 speed trains under variable speed conditions. The novelty of the research  
90 is three-fold: First, the shaft and two bearings are regarded as a coupled  
91 system in which the shaft is regarded as the rotor in this system and the  
92 mass eccentricity of the shaft is considered; Second, the angular iteration  
93 method is used to calculate the spatial position of the bearing rollers at each  
94 moment under the variable speed operation of the bearing; Third, the model  
95 is verified through a series of simulation and actual experiments with different  
96 fault modes.

97 The paper is organized as follows: Section 2 describes the process of  
98 building a shaft-bearing coupling system model under conditions of variable  
99 speed and introduces the outer ring fault, inner ring fault and rolling element  
100 fault models. Section 3 shows a few simulation results when the model has  
101 different type of fault under variable speed condition. Section 4 verifies the  
102 effectiveness of the model by comparing actual experiments and simulation  
103 experiments.

## 104 2. Bearing Model

### 105 2.1. Bearing dynamic model

106 The running part of a high-speed train consists of an axle, a left wheel,  
107 and a right wheel. According to the law of conservation of energy, the axle  
108 mass is equivalent to the axle center of mass. Fig. 1 shows the structure  
109 of the axle box bearing of high-speed trains, in which  $O_1, O_2, O_3$  are the  
110 bearing geometry center, center of shaft section and center of mass of shaft  
111 section, respectively;  $e$  is the eccentricity of cross section of the shaft,  $m_c$   
112 is the equivalent mass (kg) of the shaft at the center;  $K, C$  are the stiffness  
113 and damping of the shaft, respectively;  $F_{xL}, F_{yL}$  are the reaction force (N)  
114 received by the left end bearing in the horizontal and vertical directions,  
115 respectively,  $F_{xR}, F_{yR}$  are the reaction force (N) received by the right end

116 bearing in the horizontal and vertical directions, respectively, and  $\alpha$  and  $\beta$   
 117 are the contact angle and the half cone angle given in degree, respectively.  
 118 Since the rollers of tapered roller bearings change the direction of contact  
 119 force and decompose the load on the bearing into axial and radial directions,  
 120 the half cone angle should be considered in the model.

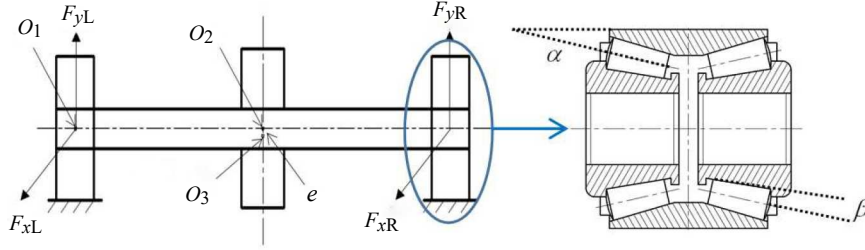


Fig. 1: Shaft and bearing coupling system model

121 Fig. 2 shows the schematic diagram of bearings dynamics model, in which  
 122  $m_1$ ,  $m_2$ ,  $m_b$  are the masses (kg) of the bearing inner ring, bearing and unit  
 123 resonator, respectively;  $x_1$ ,  $y_1$  are displacement (m) of the left row inner ring  
 124 in the horizontal and vertical directions, respectively;  $K_1$ ,  $C_1$  are support  
 125 stiffness (N/m) and support damping (N · s/m) of the inner ring, respec-  
 126 tively;  $x_2$ ,  $y_2$  are the displacement (m) of the outer ring in the horizontal  
 127 and vertical directions, respectively;  $K_2$ ,  $C_2$  are the support stiffness (N/m)  
 128 and support damping (N · s/m) of the outer ring, respectively;  $y_b$ ,  $K_b$ ,  $C_b$   
 129 are the vertical displacement (m), stiffness (N/m) and damping (N · s/m)  
 130 of the unit resonator, respectively. The bearing in Fig. 2 is considered as a  
 131 model that is coupled with a series of spring mass models and is simulated  
 132 by establishing a set of differential equations according to Newton's second  
 133 law.

134 When a fault occurs, the periodic impact of the fault leads to natural  
 135 vibration of bearing inner and outer rings and other components. The vi-  
 136 brations can be accurately simulated by adjusting the stiffness and damping  
 137 coefficient of unit resonator [19, 20]. According to Newton's second law, the  
 138 dynamics of a bearing-rotor system can be described as:

$$\begin{cases} m_c \ddot{x}_c + C \dot{x}_c + K(x_c - x_{r1}) + K(x_c - x_{l1}) = m_c e w_c^2 \cos(w_c t) \\ m_c \ddot{y}_c + C \dot{y}_c + K(y_c - y_{r1}) + K(y_c - y_{l1}) = m_c e w_c^2 \cos(w_c t) - m_c g \end{cases} \quad (1)$$

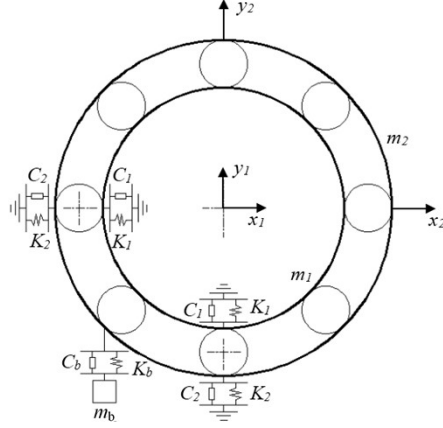


Fig. 2: Spring mass system of simplified bearings

$$\begin{cases} m_1 \ddot{x}_{r1} + C_1 \dot{x}_{r1} + K_1 x_{r1} + F_{xR} \cos(\alpha - \beta) = 0 \\ m_1 \ddot{y}_{r1} + C_1 \dot{y}_{r1} + K_1 y_{r1} + F_{yR} \cos(\alpha - \beta) = 0 \\ m_2 \ddot{x}_{r2} + C_2 \dot{x}_{r2} + K_2 x_{r2} + F_{xR} \cos(\alpha + \beta) = 0 \\ m_2 \ddot{y}_{r2} + (C_2 + C_b) \dot{y}_{r2} + (K_2 + K_b) y_{r2} - K_b y_b \\ \quad - C_b \dot{y}_b - F_{yR} \cos(\alpha + \beta) = F \cos(\alpha + \beta) \end{cases} \quad (2)$$

$$m_b \ddot{y}_{rb} + C_b (\dot{y}_{rb} - \dot{y}_{r2}) + K_b (y_{rb} - y_{r2}) = 0 \quad (3)$$

$$\begin{cases} m_1 \ddot{x}_{l1} + C_1 \dot{x}_{l1} + K_1 x_{l1} + F_{xL} \cos(\alpha - \beta) = 0 \\ m_1 \ddot{y}_{l1} + C_1 \dot{y}_{l1} + K_1 y_{l1} + F_{yL} \cos(\alpha - \beta) = 0 \\ m_2 \ddot{x}_{l2} + C_2 \dot{x}_{l2} + K_2 x_{l2} + F_{xL} \cos(\alpha + \beta) = 0 \\ m_2 \ddot{y}_{l2} + (C_2 + C_b) \dot{y}_{l2} + (K_2 + K_b) y_{l2} - K_b y_b \\ \quad - C_b \dot{y}_b - F_{yL} \cos(\alpha + \beta) = F \cos(\alpha + \beta) \end{cases} \quad (4)$$

$$m_b \ddot{y}_{lb} + C_b (\dot{y}_{lb} - \dot{y}_{l2}) + K_b (y_{lb} - y_{l2}) = 0 \quad (5)$$

139 where  $x_c$ ,  $y_c$  are the displacement of centroid of the shaft in the horizontal  
 140 and vertical directions, respectively;  $x_{r1}$ ,  $y_{r2}$  are the displacement of the outer  
 141 ring and the inner ring at the right end bearing in the horizontal direction,  
 142 respectively;  $y_{r1}$ ,  $y_{r2}$  are the displacement of the outer ring and the inner ring  
 143 at the right end bearing in the vertical direction, respectively;  $x_{l1}$ ,  $x_{l2}$ ,  $y_{l1}$ ,  $y_{l2}$   
 144 are for the left end bearing;  $y_{rb}$ ,  $y_{lb}$  are the displacement of the unit resonator

145 at right and left end in the vertical direction, respectively;  $F$  is axle load of  
146 train. In this model, Eq. (1) is the vibration equations of the shaft in the  
147 horizontal and vertical directions; Eq. (2) is the vibration equations of the  
148 right end bearing in the horizontal and vertical directions; Eq. (4) is the  
149 vibration equations of the left end bearing in the horizontal and vertical  
150 directions; Eqs. (3) and (5) are the vibration equations of the unit resonator  
151 in the vertical direction.

## 152 2.2. Bearing support reaction force

153 In the model, bearing support reaction force is needed. However, the  
154 magnitude and direction of the force change with the rotation of the bearing.  
155 The force can be calculated as follows:

- 156 1. Calculating the contact force on each roller.
- 157 2. Decomposing the force into the forward direction and radial direction  
158 of the bearing.
- 159 3. Combining all the force in the above two directions and the bearing  
160 support reaction force can be obtained in these two directions.

161 Since the forces on the inner and outer rings of bearings are transmitted  
162 through the rollers in bearing movement, the reaction force is the sum of the  
163 resultant force of the contact forces at each roller. In practice, the motion  
164 state and force of bearings are very complicated. To simplify the calculation,  
165 the following assumptions are introduced. Note that these assumptions are  
166 commonly used and do not lower the accuracy and fidelity of the model.

- 167 1. The outer ring of bearings is fixed on the rigid element with rotating  
168 velocity of 0 and it has lateral and vertical displacements.
- 169 2. The rolling elements are equidistantly located on the raceway and per-  
170 form pure rolling (i.e. sliding of rolling elements are not considered);
- 171 3. The contact stress is considered in the form of Hooke's law.

172 Fig. 3 shows the side view of a double-row tapered roller bearing with  
173  $N_0$  rollers that are equally separated by an angle of  $2\pi/N_0$ . In the rotating  
174 operation, the angle of the  $i$ -th roller ( $i = 1, 2, \dots, N_0$ ) turns at time  $t$  can be  
175 calculated as:

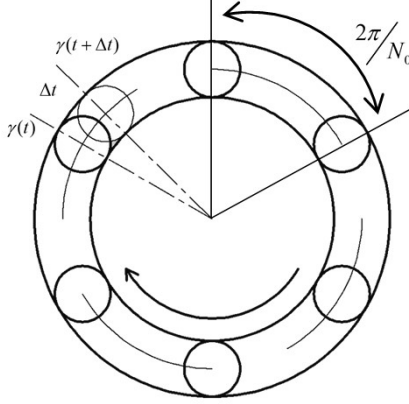


Fig. 3: Side view of a double-row tapered roller bearing

$$\theta_i = \gamma(t) + \frac{2\pi}{N_0}(i - 1), i = 1, 2, \dots, N_0 \quad (6)$$

176 where  $\gamma(t)$  is the angle that the roller indexed by 1 turns in time  $t$ , and its  
 177 initial location is  $\gamma(t_0) = 0$ . The normal contact deformation of the  $i$ -th  
 178 roller of the right end bearing with the raceway at the angular displacement  
 179  $\theta_i$  can be calculated as:

$$\delta_i = (x_{r1} - x_{r2}) \cos \theta_i + (y_{r1} - y_{r2}) \sin \theta_i - c_0 \quad (7)$$

where  $c_0$  is the bearing radial clearance. The contact force between the ball and the raceway can be expressed by the nonlinear Hertz's contact force as [21, 22]:

$$P_i = K_t \delta_i^n H_i \quad (8)$$

180 where  $K_t$  is the contact stiffness,  $n = 10/9$ . When  $\delta_i > 0$ ,  $H_i = 1$  and it  
 181 indicates that there is a nonlinear Hertz's contact force while  $\delta_i \leq 0$ ,  $H_i = 0$   
 182 indicates that there is no nonlinear Hertz's contact force. By decomposing  
 183 the contact force at every roller into the horizontal and vertical directions,  
 184 the resultant force in the two directions can be obtained. The total contact  
 185 force of the bearing in the horizontal and vertical directions is the sum of the  
 186 resultant force from all rollers, which is given as:

$$\begin{cases} F_{xR} = K_t \sum_{i=1}^{N_0} \delta_i^{\frac{10}{9}} H_i \cos \theta_i \\ F_{yR} = K_t \sum_{i=1}^{N_0} \delta_i^{\frac{10}{9}} H_i \sin \theta_i \end{cases} \quad (9)$$

187 where  $F_{xR}, F_{yR}$  are the contact force in horizontal and vertical directions,  
 188 respectively. Similarly,  $F_{xL}, F_{yL}$  can be obtained.

### 189 2.3. Model analysis with different fault modes

190 To solve the model, the angle  $\gamma(t)$  that the roller rotates at any time  
 191 instant  $t$  is needed. However, for high-speed train, the angular rotating  
 192 velocity of the main shaft  $w_0(t)$  is not a constant. To address this, we simplify  
 193 and apply the angle iteration method [17] to calculate the angle  $\gamma(t)$  in real  
 194 time.

195 The angle  $\gamma(t)$  can be calculated as:

$$\gamma(t) = \int_0^{+\infty} w_0(t)t dt \quad (10)$$

196 When the rotation speed changes with time,  $\gamma(t)$  cannot be expressed as  
 197 a linear function of time and the total angle that the roller turns at each  
 198 moment cannot be determined by the angular velocity.

199 The proposed angle iteration method assumes that the bearing speed is  
 200 piecewise constant, i.e., the speed is constant within a short period time  
 201  $\Delta t$  ( $\Delta t \rightarrow 0$ ). As a result, the angle that the bearing rotates at time  $t + \Delta t$   
 202 can be expressed as  $\gamma(t + \Delta t) = \gamma(t) + w(t)\Delta t$ , where  $w(t)$  is the relative  
 203 speed of the roller with respect to the fault location, which can be on the  
 204 outer ring, inner ring, and roller itself. Therefore,  $w(t)$  has different values  
 205 for different types of faults. When the fault is on the outer (or inner) ring,  
 206  $w(t)$  is the relative speed of the roller to the outer (or inner) ring at  $t$ . When  
 207 the fault is on the rolling element,  $w(t)$  is the rotating speed of the roller  
 208 itself at  $t$ . The schematic diagram is shown in Fig. 3. Then the problem  
 209 transforms to the estimation of  $w(t)$ . In the simulation,  $\Delta t$  represents the  
 210 step size used in each iteration of the ode45 function.

#### 211 2.3.1. Model of outer ring fault

212 Fig. 4 shows the case when the outer ring has a fault [23, 24] located in  
 213 the lower bearing area, in which  $\theta_c$  is the location of the fault center and  $\theta_{ca}$

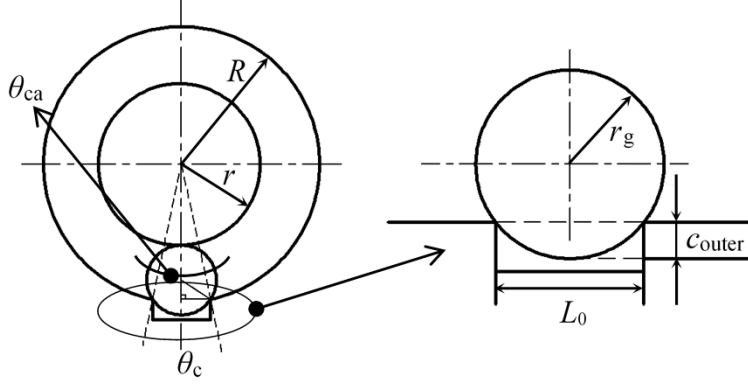


Fig. 4: Model of outer ring fault

214 is the central angle corresponding to the arc where the fault is located,  $L_0$   
 215 is the fault width,  $r$  is the inner ring radius of bearing,  $R$  is the outer ring  
 216 radius of bearing,  $r_g$  is the section radius at the center of mass of tapered  
 217 roller. When a roller rolls over the fault area, the roller descending depth  
 218  $c_{\text{outer}}$  between the roller and the raceway can be expressed by:

$$c_{\text{outer}} = \begin{cases} r_g - \sqrt{r_g^2 - \left(\frac{L_0}{2}\right)^2}, & \cos(\theta_i - \theta_c) > \cos \frac{\theta_{ca}}{2} \\ 0, & \text{else} \end{cases} \quad (11)$$

219 with  $\theta_{ca} = 2 \arcsin\left(\frac{L_0}{2R}\right)$ . Since the outer ring speed is 0, the relative speed  
 220 of the roller with respect to the outer ring  $w_{\text{outer}}(t)$  can be expressed as:

$$w(t) = w_{\text{outer}}(t) = \frac{1}{2} \left(1 - \frac{d}{D} \cos \alpha\right) w_0(t) \quad (12)$$

221 where  $d$  is the roller diameter,  $D$  is the bearing pitch diameter.

### 222 2.3.2. Model of inner ring fault

223 Fig. 5 shows the case when the inner ring of the bearing has a fault. Dif-  
 224 ferent from outer ring fault, the location of the inner ring fault continuously  
 225 changes as the bearing rotates. Because bearing cage and the inner ring have  
 226 a relative movement, the inner ring is used as the reference system, which  
 227 makes it equivalent to the form of the outer ring fault. When a roller rolls  
 228 over the fault area on the inner raceway, the roller descending depth  $c_{\text{inner}}$   
 229 between the roller and the raceway can be expressed by:

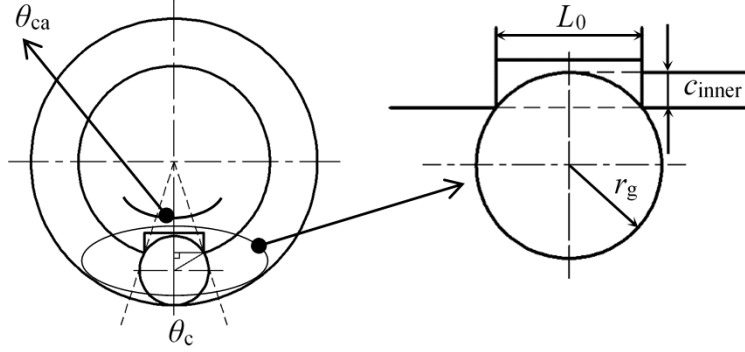


Fig. 5: Model of inner ring fault

$$c_{\text{inner}} = \begin{cases} r_g - \sqrt{r_g^2 - \left(\frac{L_0}{2}\right)^2}, & \cos(\theta_i - \theta_c) > \cos \frac{\theta_{\text{ca}}}{2} \\ 0, & \text{else} \end{cases} \quad (13)$$

230 with  $\theta_{\text{ca}} = 2 \arcsin\left(\frac{L_0}{2r}\right)$ . Then, the relative speed of the roller with respect  
 231 to the inner ring  $w_{\text{inner}}(t)$  can be calculated as:

$$w(t) = w_{\text{inner}}(t) = \frac{1}{2} \left( 1 + \frac{d}{D} \cos \alpha \right) w_0(t) \quad (14)$$

232 2.3.3. Model of rolling element fault

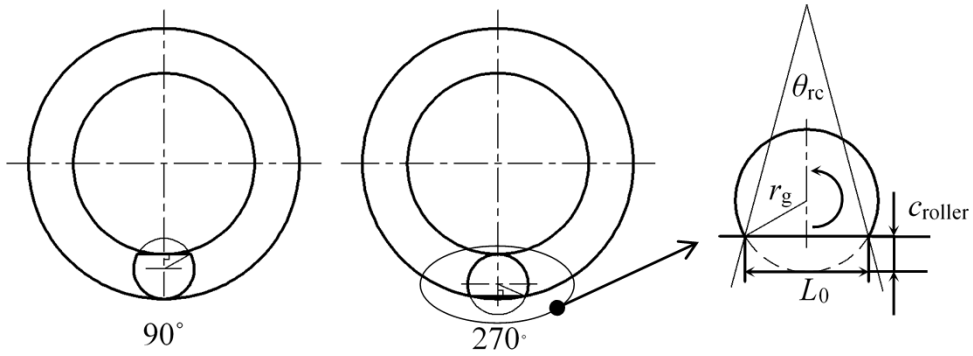


Fig. 6: Model of rolling element fault

233 Fig. 6 shows the case when a rolling element of the bearing has a fault,  
 234 in which  $\theta_{rc}$  is the central angle corresponding to the arc where the fault is  
 235 located. When the bearing has a rolling element fault, the roller contacts  
 236 the inner ring raceway and the outer ring raceway once respectively in its  
 237 own rotation cycle as the inner ring of the bearing rotates. Here, we take the  
 238 bearing cage as the reference system and assume that the initial angle of the  
 239 fault area is 0 and the rollers only have rotation (without revolution). When  
 240 the roller rotates  $90^\circ$  counterclockwise, it contacts the inner ring. When the  
 241 roller rotates  $270^\circ$  counterclockwise, it contacts outer ring. In the process,  
 242 when the roller rolls over the fault area, the roller descending depth  $c_{roller}$   
 243 can be calculated by:

$$c_{roller} = \begin{cases} r_g - \sqrt{r_g^2 - \left(\frac{L_0}{2}\right)^2}, & \cos(\theta_i - \phi) > \cos \theta_{rc} \\ 0, & else \end{cases} \quad (15)$$

where  $\phi = \pi/2$  and  $3\pi/2$  for contacting inner and outer raceways, respec-  
 tively,  $\theta_{rc} = 2 \arcsin\left(\frac{L_0}{2r_0}\right)$ , and the rotating speed of the roller  $w_{roller}(t)$  is  
 given by:

$$w(t) = w_{roller}(t) = \frac{D}{2d} \left(1 - \left(\frac{d}{D}\right)^2\right) w_0(t) \quad (16)$$

244 With above analysis, the contact deformation in the fault area under  
 245 different fault modes can be summarized as:

$$\delta_i = (x_{r1} - x_{r2}) \cos \theta_i + (y_{r1} - y_{r2}) \sin \theta_i - c_0 - c_{change} \quad (17)$$

246 where  $c_{change}$  should be  $c_{outer}$ ,  $c_{inner}$  or  $c_{roller}$ , depending on the fault mode.

### 247 3. Simulation analysis of the bearing model

#### 248 3.1. Parameters of system

249 To verify the proposed model under varying speed, a series simulations  
 250 are conducted . Tables 1, 2 and 3 list the main parameters of the high-  
 251 speed EMU axle box bearing, the rotor system, and the unit resonator in the  
 252 simulation.

Table 1: The parameter of the bearing

Parameter	Value of parameter
Inner ring mass $m_1$ (kg)	4.63
Inner ring radius $r$ (mm)	6.5
Total bearing mass $m_2$ (kg)	30
Outer ring radius $R$ (mm)	120
Number of roller $N_0$	17
Contact angle $\alpha$ ( $^\circ$ )	10
Half-cone angle $\beta$ ( $^\circ$ )	1.7
Bearing rolling element diameter $d$ (mm)	26.5
Bearing pitch meter $D$ (mm)	156.25
Axle load $F$ (N)	20250

### 253 3.2. Introduction of GATD

254 In order to verify the model, simulation results of the model need to  
255 be compared with theoretical results. First, the model is simulated under  
256 variable speed conditions to obtain the time-domain waveform of the bear-  
257 ing vibration acceleration. Then, the order ratio spectrum of the vibration  
258 is calculated for bearing diagnosis. The model is verified if the order ratio  
259 spectrum of the vibration from simulation is close to the theoretical values.  
260 Therefore, the key is to find a suitable fault diagnosis method to obtain the  
261 order ratio spectrum of bearing vibration acceleration. In 2016, Urbanek et  
262 al. [25] proposed a generalized angular temporal deterministic (GATD) signal  
263 model for rotating machinery failures under variable speed conditions, based  
264 on cyclostationary theory. This GATD signal extracted from wind turbine  
265 bearings enables the accurate identification of bearing faults. The advantage  
266 of the GATD-based method is that it does not rely on the angle resampling  
267 technology and completes the bearing fault diagnosis while retaining the orig-  
268 inal characteristics of the signal. Therefore, this paper adopts this method  
269 to extract the fault characteristics of the model simulation results.

270 The GATD-based fault diagnosis process is as follows:

Table 2: The parameter of the bearing system model

Parameter	Value of parameter
Equivalent mass at shaft center $m_c$ (kg)	274
Bending damping of shaft $C$ (N · s/m)	$2 \times 10^6$
Bending stiffness of shaft $K$ (N/m)	$1.48 \times 10^7$
Mass eccentricity of shaft section $e$ (mm)	$10^{-5}$
Inner ring damping coefficient $C_1$ (N · s/m)	7000
Inner ring stiffness coefficient $K_1$ (N/m)	$3.05 \times 10^8$
Outer ring damping coefficient $C_2$ (N · s/m)	7000
Outer ring stiffness coefficient $K_2$ (N/m)	$1.45 \times 10^{10}$
Contact stiffness coefficient $K_t$ (N/m)	$1.55 \times 10^{10}$

Table 3: The parameter of the unit resonator

Parameter	Value of parameter
Vibrator mass $m_b$ (kg)	1
Stiffness coefficient $K_b$ (N/m)	$8.8826 \times 10^9$
Damping coefficient $C_b$ (N · s/m)	9424.8

1. First, the collected faulty bearing signal  $x(t)$  is normalized according to the Z-score standardization method:

$$z_T(\varphi, f; \varphi_0) = \frac{x(t - \tau(\varphi + \varphi_0)) - \mu_T(\varphi)}{\sigma_T(\varphi)} w_T(t) \quad (18)$$

where  $\varphi(t)$  is the angle that the roller turned at time  $t$  with the initial phase  $\varphi_0$ ,  $\frac{1}{T} = \max(\frac{d\varphi}{dt})$ ,  $w_T(t)$  is a Hanning window function,  $\tau(\varphi)$  is the angle-fixed time increment used for positioning the window. Here,  $\mu_T(\varphi)$  is the local angular-temporal mean value of the signal  $x(t)$ , and  $\sigma_T(\varphi)$  is the localized angular-temporal standard deviation of  $x(t)$ ,

which are calculated as:

$$\mu_T(\varphi; \varphi_0) = \frac{1}{T} \int_{\lambda+T/2}^{\lambda-T/2} x(u) du \quad (19)$$

$$\sigma_T(\varphi; \varphi_0) = \sqrt{\frac{1}{T} \int_{\lambda+T/2}^{\lambda-T/2} (x(u) - \mu_T(\tau(\varphi)))^2 du} \quad (20)$$

271 where  $\lambda = t - \tau(\varphi + \varphi_0)$

2. Performing Fourier transform on the normalized signal:

$$Z_T(\varphi, f; \varphi_0) = \lim_{T \rightarrow \infty} \frac{1}{T} \int_0^T z_T(\varphi, t; \varphi_0) e^{-j2\pi ft} dt \quad (21)$$

3. Performing fast Fourier transform on the squared envelope spectrum of  $Z_T(\varphi, f; \varphi_0)$  to obtain the angular-temporal spectrum (ATS) of the signal:

$$ATS_T(\Omega, f, \varphi_0) = \lim_{\Theta \rightarrow \infty} \frac{1}{\Theta} \int_0^\Theta |Z_T|^2 e^{-j2\pi\Omega\varphi} d\varphi \quad (22)$$

272 where  $Z_T$  denotes  $Z_T(\varphi, t; \varphi_0)$  to simplify the notation,  $\Omega$  is the fre-  
 273 quency related to angle-fixed events (expressed in orders),  $f$  denotes  
 274 events occurring frequency in Hz, and  $\Theta$  is the maximum angle pe-  
 275 riod. The obtained *ATS* is a family of curves distributed in the three-  
 276 dimensional (3-D) space, and the order ratio spectrum of the signal can  
 277 be obtained by plotting with  $\Omega$  as the horizontal axis.

### 278 3.3. Model simulation

According to theoretical mechanics, the fault characteristic order ratio of the outer ring, the inner ring and the rolling element can be respectively calculated by [26]:

$$f_o = \frac{N_0}{2} \times \left( 1 - \frac{d}{D} \cos \alpha \right) \quad (23)$$

$$f_i = \frac{N_0}{2} \times \left( 1 + \frac{d}{D} \cos \alpha \right) \quad (24)$$

$$f_r = \frac{1}{2} \times \frac{D}{d} \left( 1 + \left( \frac{d}{D} \cos \alpha \right)^2 \right) \quad (25)$$

279 For the bearing used in this research, we have  $f_o = 7.082$ ,  $f_i = 9.917$ , and  
 280  $f_r = 2.871$ .

281 The simulation is conducted in Matlab with a sampling frequency of  
 282 512,000 Hz. The angular rotating velocity of the main shaft  $w_0(t)$  is given in  
 283 Eq. (26) and shown in Fig. 7. This speed is designed to simulate the entire  
 284 operating process of the bearing system that contains accelerating process,  
 285 decelerating process and oscillating process with a sine law. Three simula-  
 286 tions are conducted with three types of faults, an outer ring fault, an inner  
 287 ring fault, and a rolling element fault, all with a fault size  $L_0 = 1$  mm.

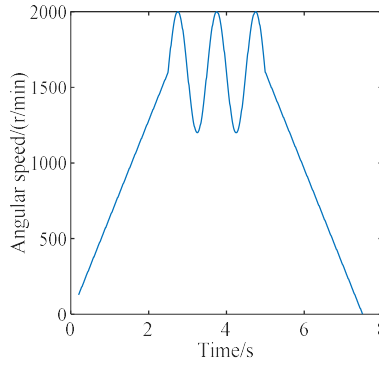


Fig. 7: Angular speed of bearings inner ring

$$w_0(t) = \begin{cases} 640t & 0.2 < t \leq 2.5 \\ 1600 + 400 \sin(\pi(t - 2.5)) & 2.5 < t \leq 5 \\ 4800 - 640t & 5 < t \leq 7.5 \end{cases} \quad (26)$$

288 From the solution of Eqs. (1)-(5), the order ratio spectrum analysis  
 289 method in [25] is used to obtain the corresponding order ratio spectrum.  
 290 The time-domain waveform of the acceleration of bearings and the corre-  
 291 sponding order ratio spectrum are respectively obtained by simulating the  
 292 model when an outer ring, an inner ring, and a rolling element fault with  
 293  $L_0 = 1$  mm, respectively. Fig. 8-Fig. 10 show the results.

294 It can be seen intuitively from the three time domain graph that when  
 295 a fault occurs, the acceleration amplitude of the bearing changes with the  
 296 trend of shaft angular speed. In addition, the maximum amplitude increases  
 297 in order according to the types of the faults, which means the location of  
 298 the fault has different effects on the vibration of bearing. Apparently, when  
 299 a fault is on the rolling elements, the bearing has the severest vibration.

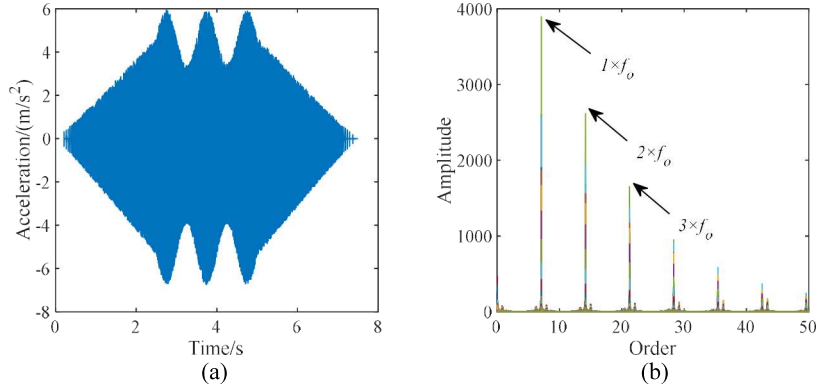


Fig. 8: Vibration with outer ring fault (a) Vibration signal and (b) order ratio spectrum

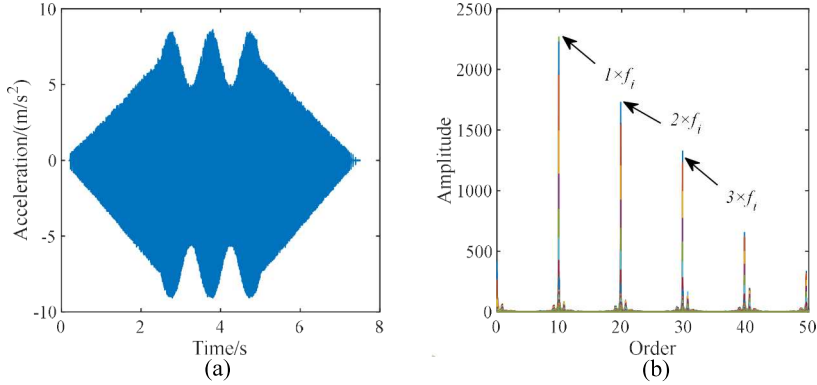


Fig. 9: Vibration with inner ring fault (a) Vibration signal and (b) order ratio spectrum

300 Moreover, the results show that the simulated characteristic order ratios of  
 301 the outer ring (7.805), inner ring (9.9172), and rolling element (2.8694) are  
 302 close to the calculation results given by Eq. (23)-(25). At the same time, the  
 303 corresponding frequency multiplication can be observed in the order ratio  
 304 spectrum, which proves the correctness of the model.

305 Since the order ratio spectrum is obtained by the signal after two Fourier  
 306 transforms, there is a linear relationship between the order ratio spectrum  
 307 amplitude and the original signal amplitude. Letting the amplitude corre-  
 308 sponding to the single frequency (ACSF) in the signal order ratio spectrum  
 309 under an outer ring fault and an inner ring fault are  $A_o$  and  $A_i$ , respectively.  
 310 The influence of the fault location and the fault size on the ACSF is studied  
 311 and the results are shown in Fig. 11.

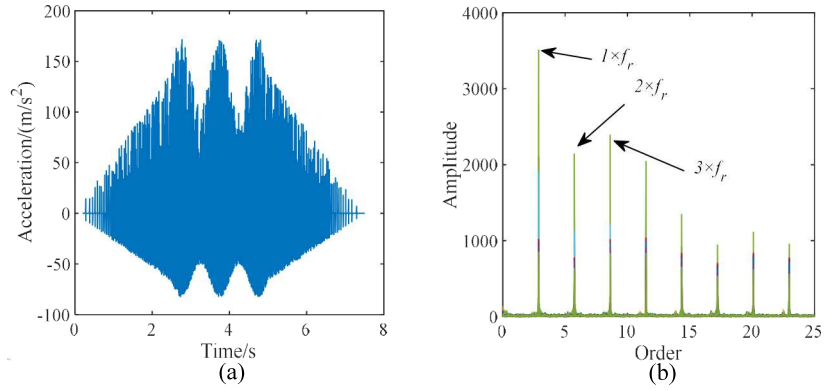


Fig. 10: Vibration with rolling element fault (a) Vibration signal and (b) order ratio spectrum

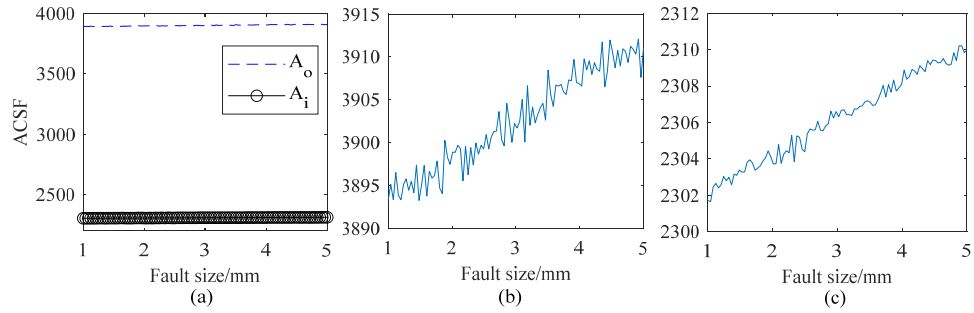


Fig. 11: Result of amplitude change with fault size

312 Fig. 11(a) shows the ACSF values under outer ring is always larger than  
 313 that under inner ring. Fig. 11(b) and (c) show that the ACSF values in the  
 314 order ratio spectrum under these two fault conditions increase as the fault  
 315 sizes increases, which indicates that the fault size has an important influence  
 316 on the motion state of the bearing. As the size of the fault increases, more  
 317 energy is generated in the fault area when the roller collides with the raceway,  
 318 which causes the increase of the amplitude at this frequency.

#### 319 4. Experimental verification

320 To make the operating condition close to real operation, the experiments  
 321 use a speed profile in which the bearing rotating speed is accelerated from 0  
 322 to a certain speed, maintained for a period of time, and then decelerated to

323 0. It is important to note that, in the experiments, tachometer is not used  
324 to measure the speed of the bearing and no program is used to control its  
325 speed. For the faulty type verification, the vibration is from experiment and  
326 speed profile is not needed. However, the speed profile is used as the model  
327 input for the bearing operating condition verification. Since the model speed  
328 profile is unknown, the instantaneous speed of the bearing must be estimated  
329 from the bearing vibration signals.

#### 330 4.1. Fault type verification

331 Two EMU axle box bearings are used in the experiments. One bearing  
332 has a through-groove fault on the outer ring with the width of  $L_0=1$  mm and  
333 the other one has a pitting fault on the inner ring with  $L_0=0.1$  mm. The  
334 schematic diagram of the outer ring, the fault on the outer ring, and the fault  
335 on the inner ring are shown in Fig. 12. In the experiments, the vibration  
336 signal of the bearing is collected in 60 s with a sampling frequency of 51,200  
337 Hz.

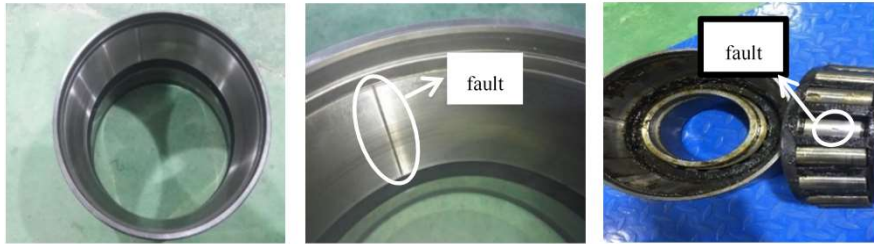


Fig. 12: The outer ring, outer ring fault, and inner ring fault of the bearing

338 The acceleration sensors should be installed near the experimental bearing  
339 so that the vibration signal can be accurately measured. Fig. 13 shows the  
340 experimental platform and the horizontal and vertical location of the sensors.

341 Experiments are carried out on the bearings with seeded faults. For the  
342 bearing with the outer ring fault, Fig. 14 shows the time domain signal and  
343 the order ratio spectrum of the bearing vibration acceleration. It can be seen  
344 that the difference of the experimental results and the calculation results of  
345 the first three-order fault feature order ratio are respectively 5.97%, 5.67%  
346 and 6.34%.

347 For the bearing with an inner ring fault, Fig. 15 shows the time domain  
348 signal and order ratio spectrum of the bearing vibration acceleration. The

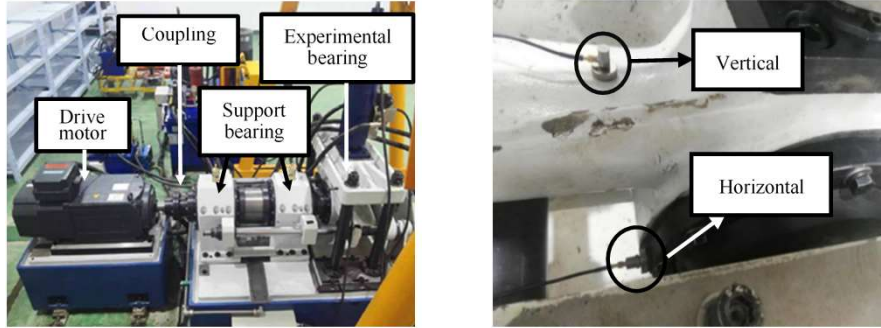


Fig. 13: Test rig of roller bearing of railway vehicle and sensors' location

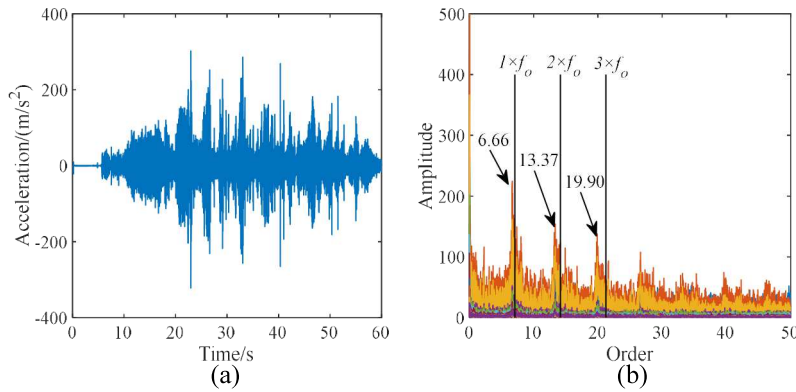


Fig. 14: Vibration with outer ring (a) Time domain vibration signal, (b) order ratio spectrum

349 difference of the experimental results and the calculation results of the first  
 350 three-order fault feature order ratio are respectively 2.59%, 3.95% and 4.15%.

351 As mentioned early, the bearing speed is changing in the experiments.  
 352 Under these non-linear operating conditions, the acceleration amplitude of  
 353 the bearing changes continuously with time, which is a typical variable speed  
 354 bearing operation for high-speed trains. The results show that, compared  
 355 with the theoretical value given by Eq. (23)-(24), the difference of the fault  
 356 characteristic order ratio under two experimental conditions are within the  
 357 allowable range, which proves the effectiveness of the model.

#### 358 4.2. Bearing operating conditions verification

359 In order to further prove that the model is also effective in real work-  
 360 ing conditions and has a certain anti-interference ability against noise, the

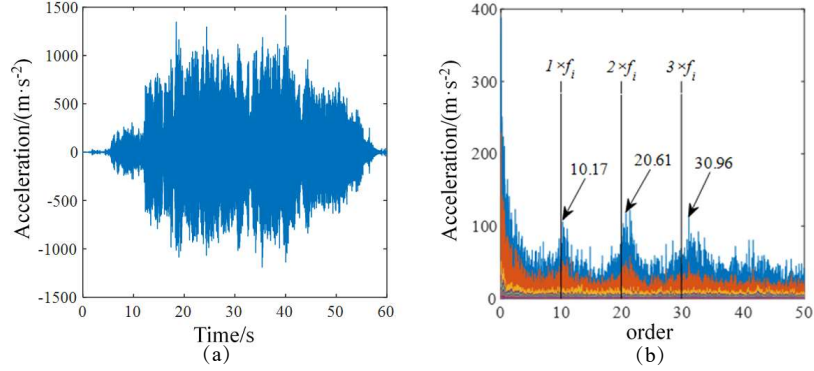


Fig. 15: Vibration with inner ring (a) Time domain vibration signal, (b) order ratio spectrum

361 bearing speed estimated in the experiment is used as the input of the model  
 362 and noise is added to the bearing vibration acceleration signal obtained from  
 363 the model. The order ratio spectrum analysis is performed on the model  
 364 output vibration signal with noise. If the model result is consistent with the  
 365 calculation result, the model is verified.

366 Since there is no speed measuring device, such as a tachometer, and  
 367 speed profile is unknown, the real-time speed of the bearing spindle cannot  
 368 be obtained. Therefore, this study extracts the instantaneous speed curve  
 369 from the signals collected in the two experiments, and uses a time function  
 370 to fit this two working conditions for model speed input. At the same time,  
 371 on-site noise is added to the model to make the simulation close to a real  
 372 noisy environment.

#### 373 4.2.1. Verification under outer ring fault

374 The speed curve is extracted from the experimental signals by the method  
 375 in [27], and the noise signal is extracted from the signal using the wavelet  
 376 noise reduction method [28]. Fig. 16 shows the instantaneous speed and  
 377 experimental site noise extracted from the outer ring fault test signal. The  
 378 fitted curve function is  $f(t) = -0.002t^4 + 0.2535t^3 - 11.7572t^2 + 232.4658t -$   
 379  $2.0618 \times 10^{-4}$ .

380 It can be seen that the bearing speed experiences a process of speed  
 381 increase, slowly change, and decrease during the experiment. Meanwhile,  
 382 the noise amplitude experience the same process as well.

383 With the proposed model, the fitted speed curve, and the noise, Fig.

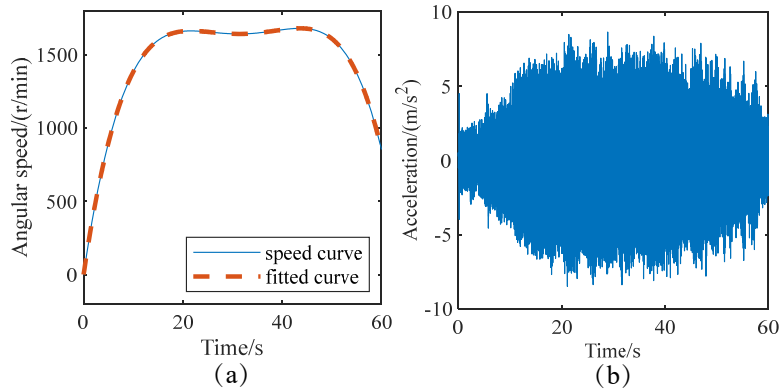


Fig. 16: Experimental signal under outer ring fault (a) speed curve, (b) site noise

384 17(a) shows the vibration signal obtained from the model. The order ratio  
 385 spectrum in Fig. 17(b) shows that the values of frequency-singled, frequency-  
 386 doubled and frequency-tripled are close to the theoretical values given by Eq.  
 387 (23). The results demonstrate the effectiveness of the model.

#### 388 4.2.2. Verification under inner ring fault

389 The same methods are used to obtain the time frequency curve and ex-  
 390 perimental site noise in inner ring fault experiment. Fig. 18 shows the in-  
 391 stantaneous speed and experimental site noise extracted from the inner ring  
 392 fault test signal. The fitted curve function is  $f(t) = -0.0028t^4 + 0.3423t^3 -$   
 393  $14.3913t^2 + 251.987t - 6.0213 \times 10^{-4}$ .

394 With the proposed model, the vibration signal of the model shown in Fig.  
 395 19(a) under the fitted speed profile given in Fig. 18(a) can be obtained. The  
 396 order ratio spectrum in Fig. 19(b) shows that the values of frequency-singled,  
 397 frequency-doubled and frequency-tripled are close to the theoretical values  
 398 given by Eq. (24). The results demonstrate the effectiveness of the model.

399 It is noticed that the ACSF values under outer ring fault is smaller. The  
 400 reason is that, when the bearing speed changes, the instantaneous impact  
 401 load and amplitude caused by a single fault are reduced. Meanwhile, There  
 402 are very few messy frequency components in the order ratio spectrum, which  
 403 proves that the model has good anti-interference ability. Even if the ex-  
 404 perimental site noise is added, the simulation model can get very obvious  
 405 results.

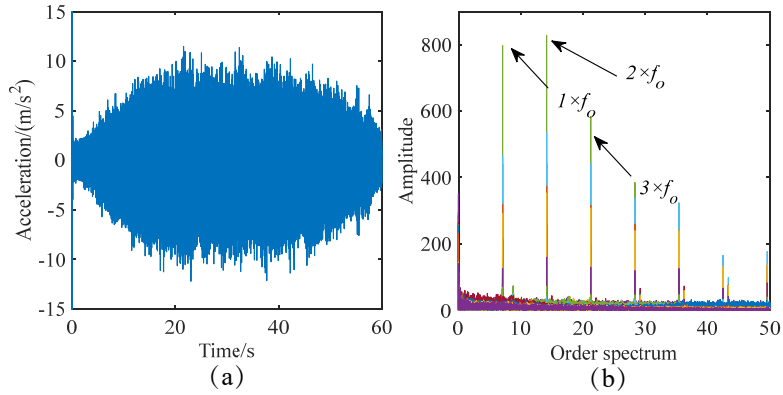


Fig. 17: Simulation results of bearing with outer ring fault (a) vibration acceleration, (b) order ratio spectrum

## 406 5. Conclusion

407 This paper establishes a dynamic model of bearing systems in the run-  
 408 ning part of high-speed trains under variable speed conditions. The novelty is  
 409 that an angle iteration method is used to address the problem that the roller  
 410 space position cannot be determined in bearing rotation, which is ignored in  
 411 the existing researches. By simulating the actual operating conditions of the  
 412 train, the vibration response of the system in the process of speed increase,  
 413 decrease and speed oscillation is obtained. The results show that the vibra-  
 414 tion acceleration amplitude of bearing outer ring is positively correlated with  
 415 bearings spindle speed. To demonstrate the effectiveness of the model, bear-  
 416 ing experiments and simulations under outer ring fault and inner ring fault  
 417 with varying speed are conducted. The order ratio of the fault character-  
 418 istics show that the errors between the simulation and experimental results  
 419 are always within the allowable range, which demonstrate the effectiveness  
 420 of the model.

## 421 Acknowledgement

422 The authors would like to thank X Gu, W Liu and L Zhao for their work  
 423 on the fault bearing experiment of high-speed train. Many thanks to the  
 424 anonymous reviewers, who provided valuable feedback and recommendations.

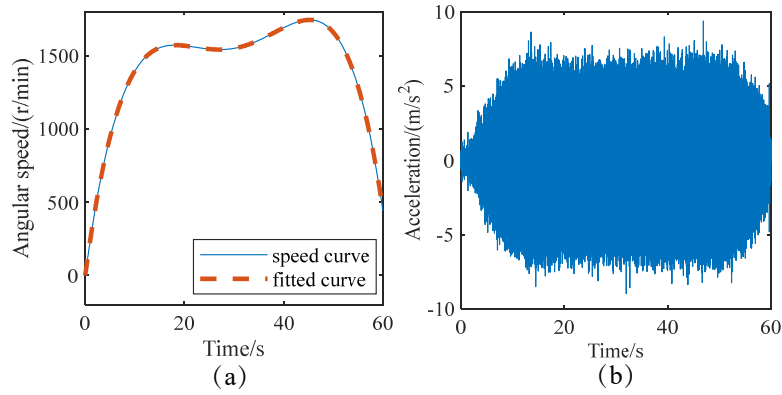


Fig. 18: Experimental signal under inner ring fault (a) speed curve, (b) site noise

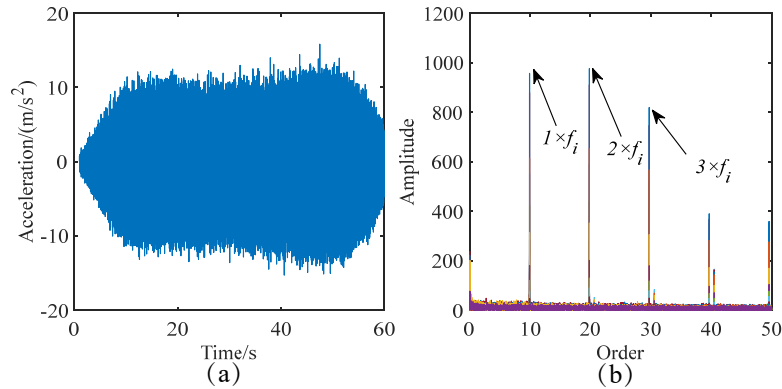


Fig. 19: Simulation results of bearing with inner ring fault (a) vibration acceleration, (b) order ratio spectrum

425 **Authors' contributions**

426 Yongqiang Liu: Validation, Resources, Writting- Reviewing and Editing.

427 Baosen Wang: Conceptualization, Methodology, Coding, Writting- Original draft and Editing.

429 Bin Zhang: Conceptualization, Resources, Investigation, Writting- Reviewing and Editing.

431 Shaopu Yang: Validation, Writting- Reviewing and Editing.

432 **Authors' information**

433 Yongqiang Liu, born in 1983, is currently a professor at School of Me-  
434chanical Engineering, Shijiazhuang Tiedao University, China. He received his  
435 PhD degree in vehicle engineering from Beijing Jiaotong University, China,  
436 in 2011. His research interests include prognostics and health management,  
437 vehicle system dynamics, and smart soft material and damper.

438 Baosen Wang, born in 1990, is currently a PhD candidate at School of  
439 Traffic and Transportation, Shijiazhuang Tiedao University, China. He re-  
440 ceived his master's degree from Shijiazhuang Tiedao University, China, in  
441 2018. His research interests include dynamic modeling analysis and bearing  
442 fault diagnosis of high-speed train bearings.

443 Bin Zhang, born in 1972, is currently an associate professor at Department  
444 of Electrical Engineering, University of South Carolina, USA. He received his  
445 PhD degree in electrical engineering from Nanyang Technological University,  
446 Singapore, in 2007. His research interests include prognostics and health  
447 management, intelligent systems and controls, and their applications to var-  
448 ious engineering systems.

449 Shaopu Yang, born in 1962, is currently a professor at State Key Labora-  
450 tory of Mechanical Behavior and System Safety of Traffic Engineering Struc-  
451 tures, Shijiazhuang Tiedao University, China. He received his PhD degree  
452 in mechanics from Tianjin University, China, in 1991. His research interests  
453 include dynamics and control of vehicle system, theory and application of  
454 nonlinear system dynamics and control.

455 **Funding**

456 Supported by the National Natural Science Foundation of China  
457 (Nos. 11790282,12032017,11802184,11902205 and 12002221), S&T Program  
458 of Hebei (20310803D), and Natural Science Foundation of Hebei Province  
459 (No A2020210028), Postgraduates Innovation Foundation of Hebei Province  
460 (CXZZBS2019154), and State Foundation for Studying Abroad.

461 **Competing interests**

462 The authors declare no competing financial interests.

463 **Author Details**

- 464 1. School of Mechanical Engineering, Shijiazhuang Tiedao University,  
465 Shijiazhuang, 050043, China.
- 466 2. School of Traffic and Transportation, Shijiazhuang Tiedao University, Shi-  
467 jiazhuang, 050043, China.
- 468 3. College of engineering and computing, University of South Carolina,  
469 Columbia, South Carolina, 29208, America.
- 470 4. State Key Laboratory of Mechanical Behavior and System Safety of  
471 Traffic Engineering Structures, Shijiazhuang Tiedao University, Shijiazhuang  
472 050043, China.

473 **References**

- 474 [1] J.-W. Yang, J.-H. Wang, Q. Huang, M. Zhou, Reliability assessment  
475 for the solenoid valve of a high-speed train braking system under small  
476 sample size, *Chinese Journal of Mechanical Engineering* 31 (2018) 1–11.
- 477 [2] Y. Yu, J. Liu, B. Ye, G. Yu, X. Jin, L. Sun, J. Tong, Design and  
478 experimental research on seedling pick-up mechanism of planetary gear  
479 train with combined non-circular gear transmission, *Chinese Journal of*  
480 *Mechanical Engineering* 32 (2019) 1–13.
- 481 [3] Z. Shang, W. Li, M. Gao, X. Liu, Y. Yu, An intelligent fault diagnosis  
482 method of multi-scale deep feature fusion based on information entropy,  
483 *Chinese Journal of Mechanical Engineering* 34 (2021) 1–16.
- 484 [4] M. Chinta, A. Palazzolo, Stability and bifurcation of rotor motion in a  
485 magnetic bearing, *Journal of sound and vibration* 214 (1998) 793–803.
- 486 [5] J.-J. Sinou, Non-linear dynamics and contacts of an unbalanced flexible  
487 rotor supported on ball bearings, *Mechanism and Machine Theory* 44  
488 (2009) 1713–1732.
- 489 [6] S. Fukata, E. H. Gad, T. Kondou, T. Ayabe, H. Tamura, On the radial  
490 vibration of ball bearings: computer simulation, *Bulletin of JSME* 28  
491 (1985) 899–904.
- 492 [7] M. Tiwari, K. Gupta, O. Prakash, Effect of radial internal clearance of  
493 a ball bearing on the dynamics of a balanced horizontal rotor, *Journal*  
494 *of sound and vibration* 238 (2000) 723–756.

- 495 [8] N. Sawalhi, R. Randall, Simulating gear and bearing interactions in the  
496 presence of faults: Part i. the combined gear bearing dynamic model  
497 and the simulation of localised bearing faults, *Mechanical Systems and*  
498 *Signal Processing* 22 (2008) 1924–1951.
- 499 [9] N. Sawalhi, R. Randall, Simulating gear and bearing interactions in the  
500 presence of faults: Part ii: Simulation of the vibrations produced by  
501 extended bearing faults, *Mechanical Systems and Signal Processing* 22  
502 (2008) 1952–1966.
- 503 [10] N. A. H. Tsuha, K. L. Cavalca, Stiffness and damping of elasto-hydrody-  
504 namic line contact applied to cylindrical roller bearing dynamic model,  
505 *Journal of Sound and Vibration* (2020) 115444.
- 506 [11] S. Xi, H. Cao, X. Chen, Dynamic modeling of spindle bearing system  
507 and vibration response investigation, *Mechanical Systems and Signal*  
508 *Processing* 114 (2019) 486–511.
- 509 [12] Q. Cao, X. Guo, G. Xiong, Research on dynamic characteristics of  
510 loose support system of rolling bearing of high-speed train, *Mechanical*  
511 *Engineering* 52 (2016) 87–95.
- 512 [13] H. Cao, Z. He, Y. Zi, Mechanical characteristic modeling and damage  
513 mechanism analysis of high-speed rolling bearings, *Chinese Vibration*  
514 *Engineering Society* 31 (2012) 134–140.
- 515 [14] t. Yang, Q. Ding, T. Guo, Vibration characteristics analysis of local fault  
516 on emu train bogie bearing, *Vibration Measurement and Diagnosis* 36  
517 (2016) 665–673.
- 518 [15] Y. Liu, B. Wang, S. Yang, Nonlinear dynamic behaviors analysis of  
519 bearings rotor system with outer ring faults in the high-speed train,  
520 *Mechanical Engineering* 54 (2018) 17–25.
- 521 [16] Z. Wang, Y. Song, Z. Yin, R. Wang, W. Zhang, Random response  
522 analysis of axle-box bearing of a high-speed train excited by crosswinds  
523 and track irregularities, *IEEE Transactions on Vehicular Technology* 68  
524 (2019) 10607–10617.

- 525 [17] C. Mishra, G. Chakraborty, A. K. Samantaray, Rolling element bearing  
526 fault modelling to develop a diagnosis scheme for oscillating and non-  
527 uniform shaft rotation, *Proc. INACOMM 2013* (2013) 86–94.
- 528 [18] C. Mishra, A. Samantaray, G. Chakraborty, Bond graph modeling and  
529 experimental verification of a novel scheme for fault diagnosis of rolling  
530 element bearings in special operating conditions, *Journal of Sound and  
531 Vibration* 377 (2016) 302–330.
- 532 [19] L. Ma, J.-h. Zhang, J.-w. Lin, J. Wang, X. Lu, Dynamic characteristics  
533 analysis of a misaligned rotor-bearing system with squeeze film dampers,  
534 *Journal of Zhejiang University-SCIENCE A* 17 (2016) 614–631.
- 535 [20] L. Cui, Y. Zhang, F. Zhang, J. Zhang, S. Lee, Vibration response  
536 mechanism of faulty outer race rolling element bearings for quantitative  
537 analysis, *Journal of Sound and Vibration* 364 (2016) 67–76.
- 538 [21] Y. Qin, F. Cao, Y. Wang, W. Chen, H. Chen, Dynamics modelling  
539 for deep groove ball bearings with local faults based on coupled and  
540 segmented displacement excitation, *Journal of Sound and Vibration*  
541 447 (2019) 1–19.
- 542 [22] D. Xiang, Y. Shen, Y. Wei, A contact force model considering meshing  
543 and collision states for dynamic analysis in helical gear system, *Chinese  
544 Journal of Mechanical Engineering* 32 (2019) 1–12.
- 545 [23] Y. Jiang, W. Huang, J. Luo, W. Wang, An improved dynamic model of  
546 defective bearings considering the three-dimensional geometric relation-  
547 ship between the rolling element and defect area, *Mechanical Systems  
548 and Signal Processing* 129 (2019) 694–716.
- 549 [24] A. M. Ahmadi, D. Petersen, C. Howard, A nonlinear dynamic vibration  
550 model of defective bearings—the importance of modelling the finite size  
551 of rolling elements, *Mechanical Systems and Signal Processing* 52 (2015)  
552 309–326.
- 553 [25] J. Urbanek, T. Barszcz, A. Jablonski, Application of angular–temporal  
554 spectrum to exploratory analysis of generalized angular–temporal deter-  
555 ministic signals, *Applied Acoustics* 109 (2016) 27–36.

- 556 [26] Y. Hu, X. Tu, F. Li, H. Li, G. Meng, An adaptive and tacholeless or-  
557 der analysis method based on enhanced empirical wavelet transform for  
558 fault detection of bearings with varying speeds, *Journal of Sound and*  
559 *Vibration* 409 (2017) 241–255.
- 560 [27] Y. Yang, Z. Peng, G. Meng, W. Zhang, Spline-kernelled chirplet trans-  
561 form for the analysis of signals with time-varying frequency and its ap-  
562 plication, *IEEE Transactions on Industrial Electronics* 59 (2011) 1612–  
563 1621.
- 564 [28] S. Wen, W.-S. Gan, D. Shi, An improved selective active noise control  
565 algorithm based on empirical wavelet transform, in: *ICASSP 2020-*  
566 *2020 IEEE International Conference on Acoustics, Speech and Signal*  
567 *Processing (ICASSP)*, IEEE, 2020, pp. 1633–1637.